Wave Runup Over Steep Rocky Cliffs

G. Dodet, F. Leckler, Damien Sous, Fabrice Ardhuin, J F Filipot, S. Suanez

SPi	Journal Code:				Article ID	Dispatch: 22.09.18	CE: RFS
	J	G	R	C	23134	No. of Pages: 21	ME:

Revised proofs are sent only in the case of extensive corrections upon request.

AGU100 ADVANCING EARTH AND SPACE SCIENCE

JGR

Journal of Geophysical Research: Oceans

RESEARCH ARTICLE

10.1029/2018JC013967

Key Points:
- Wave runup is measured over steep rocky cliffs with pressure sensors
- Wave runup shows a linear dependence to the square root of the offshore waveheight times the offshore wavelength
- Regression analysis reveals a significantly reduced runup compared to sandy environments that is attributed to enhanced bottom friction

Supporting Information:
- Supporting Information S1
- Data Set S1
- Data Set S2
- Data Set S3
- Data Set S4
- Data Set S5
- Data Set S6
- Data Set S7

Correspondence to:
G. Dodet,
guillaume.dodet@univ-brest.fr

Citation:
Dodet, G., Leckler, F., Sous, D., Ardhuin, F., Filipot, J.-F., & Suanez, S. (2018) Wave runup over steep rocky cliffs. *Journal of Geophysical Research: Oceans*, *123*. https://doi.org/10.1029/2018JC013967

Received 9 MAR 2018
Accepted 13 SEP 2018
Accepted article online 17 SEP 2018

Wave Runup Over Steep Rocky Cliffs

G. Dodet[1], F. Leckler[2], D. Sous[3], F. Ardhuin[4], J.F. Filipot[5], and S. Suanez[1]

[1]Université de Bretagne Occidentale, CNRS, Brest, France, [2]Département Recherche, Shom, Brest, France, [3]Université de Toulon, Aix-Marseille Université, CNRS, INSU, IRD, MIO, UM110, Marseille, France, [4]Université de Bretagne Occidentale, CNRS, IRD, Ifremer, UMR LOPS, IUEM, Brest, France, [5]France Energies Marines, Technopôle Brest-Iroise, Brest, France

Abstract Wave runup is known to depend on offshore wave conditions and coastal morphology. While most field studies on wave runup have focused on low-to-mild-sloping sandy beaches, runup measurements on steep and irregular rocky cliff profiles are still very scarce. Here we investigate the physical processes controlling wave runup in such environments and the range of applicability of empirical runup formula. This study focuses on the steep rocky cliffs ($0.1 < \tan\beta < 0.4$) of Banneg Island, a small island located in the Molène archipelago, Brittany, France, occasionally flooded during extreme water level events. A statistical parameter for extreme runup is derived from the measurements of pressure sensors deployed in the intertidal zone. Deep water wave parameters are used to force a high-resolution wave model, and nearshore wave parameters and high-resolution topographic data are analyzed concurrently with runup time series in order to assess the dependence of the runup on hydrodynamic conditions and morphological parameters. The wave runup is shown to be strongly related to the square root of the offshore significant wave height times the offshore wavelength. The measurements also reveal the depth dependence of the runup, which is mainly attributed to the curvature of the foreshore profile. In comparison to empirical relation obtained for a mild-sloping beach, the present data show a significant reduction in normalized wave runup, that is attributed to enhanced bottom friction over the rocky bottom.

Plain Language Summary When waves reach the shores, they travel up and down the beach before being reflected seaward. The maximum vertical excursion of the waterline relative to the still water level, called the wave runup, is a key parameter for the design of coastal structures and the prediction of overtopping volumes during storm events. Most runup studies in natural environments have focused on smooth and mild-sloping sandy beaches, and empirical formula to predict the wave runup has been derived for these environments. Here we study the process of wave runup over steep rocky cliffs. Using pressure sensors deployed in the intertidal zone of Banneg Island—a small island located west of Brittany, France, exposed to very high waves—we measured runup events. Then we investigated the link between these runup data, offshore wave parameters, and cliff slopes. Our results reveal that the wave runup is linearly dependent to the square root of the offshore wave height times the offshore wavelength. In addition, a significant reduction of the runup is found compared to sandy environments, which is attributed to the frictional effect exerted by the rocky bottom on the flow.

1. Introduction

Determining the maximum wave runup during storm conditions is of crucial importance for the design of coastal engineering structures and the management of coastal hazards of hydrodynamic and/or morphodynamic nature. Hence, for more than half a century, researchers and coastal engineers have investigated the link between wave runup and environmental parameters. In a pioneering study, Hunt (1959) analyzed laboratory data and found a linear relationship between the normalized wave runup and the foreshore slope divided by the offshore wave steepness (named the surf similarity parameter, ξ_0, by Battjes, 1974). This relationship can be written

$$\frac{R}{H_0} = K\frac{\tan\beta}{\sqrt{H_0/L_0}} = K\xi_0, \tag{1}$$

where R is the wave runup, H_0 is the offshore significant wave height, K is a nondimensional constant, β is the slope of the structure, and L_0 is the offshore wave length. Later, Holman (1986) analyzed video-based

measurements of wave runup over a natural sandy beach and found similar linear relationships for extreme statistical runup parameters, such as the 2% exceedance level of shoreline elevation η_2 or the 2% exceedance level of runup maxima R_2. Stockdon et al. (2006) analyzed a large collection of field data and showed that the extreme wave runup R_2 could be decomposed into a steady component, the wave setup, and a fluctuation about this setup, the swash. They also decomposed the significant swash height into incident and infragravity frequency bands and showed that the dimensional incident swash scaled well with $\xi_0 H_0 = \tan\beta\sqrt{H_0 L_0}$, while the dimensional infragravity swash better scaled with $\sqrt{H_0 L_0}$. As a consequence, two runup parameterizations were proposed by these authors: one for dissipative conditions, where infragravity swash dominates and slope effects can be ignored, and one for intermediate and reflective conditions, where incident swash also contributes to the runup and slope effects are included.

Most field measurements of wave runup were collected on sandy beaches, with foreshore slopes ranging from 0.02 to 0.2 (Atkinson et al., 2017; Guza & Thornton, 1982; Holland et al., 1995; Holman & Guza, 1984; Huntley et al., 1977; Raubenheimer & Guza, 1996; Ruessink et al., 1998; Senechal et al., 2011; Vousdoukas et al., 2012), and very few field data exist for steeper environments (>0.2). Poate et al. (2016) analyzed video-based runup measurements on gravel beaches, with slopes up to 0.4. They obtained strong correlations between the wave runup and the offshore significant wave height, the mean wave period, the beach slope, and the grain size, in decreasing order of importance. They also found that the widely used runup equation of Stockdon et al. (2006) strongly underestimated the runup when it was applied to their field conditions. They related this amplification of runup to the steep planar slopes of gravel beaches that extend well into the subtidal region and can maintain reflective conditions even under the most energetic conditions. For natural steep rocky cliffs, the dynamics is expected to become even more complex with the higher reflection due to increased steepness (Poate et al., 2016), the stronger dissipation due to increased bottom drag, enhanced turbulence during the breaking processes affected by impacts, splash-ups, and air entrapment (Sambe et al., 2011), and the volume loss of the swash tongue due to infiltration within fractured bed rock. Due to the harshness of the considered environment, these processes are still poorly understood, and no runup data have been published on these environments, to the knowledge of the authors. However, several laboratory studies have investigated the propagation of wave runup over artificial breakwaters for design purpose. Hunt (1959), and later Van der Meer and Stam (1992), compared runup measurements over smooth and rough structures and showed that the runup on rock slopes could be reduced by up to 50% in comparison to the runup on smooth slopes, due to enhanced bottom drag forces. Therefore, they added a correction factor to equation (1) in order to take into account the effect of bottom roughness on the wave runup. This correction is also mentioned by Van der Meer et al. (2016), and recent detailed measurements and simulations have confirmed the influence of bottom friction on swash hydrodynamics (Torres-Freyermuth et al., 2013).

The present study investigates the relationship between wave runup, wave parameters, and foreshore morphology for steep rocky cliffs in order to understand its variability and test whether the relationship derived for sandy beaches or artificial breakwaters could apply to these specific environments. We use field data recorded during three consecutive winters between 2012 and 2015 on Banneg Island, a small uninhabited island of the Molène archipelago, Brittany, France, episodically flooded during storms. In section 2, we describe the environmental context of the island and the field survey. Section 3 presents the methods that we used to simulate the nearshore wave parameters and to compute the cliff slopes and the extreme runup statistics inferred from the pressure sensor records. A major methodological issue of our study is to allow a robust detection of runup parameters in such rugged terrain where pressure distribution in the water column is expected to show significant departures from hydrostaticity. In section 4, we compare the estimated runup time series with incident wave conditions and foreshore slopes, computed on various segments of the cliff profile. Finally, we propose a more general discussion on wave runup in rocky cliff environments, including the involved physical processes, an estimation of the static (setup), infragravity and incident components, and the relationship with surf-similarity parameter (section 5).

2. Banneg Island

2.1. Geomorphological Context and Hydrodynamic Conditions

Banneg Island is located off the western tip of the Brittany peninsula, in France (Figure 1a). It lies in the north-western edge of the Molène archipelago, which is separated from Ouessant Island by the 60-m-deep Fromveur Channel (Figure 1b). This small island is oriented north-south, 0.8 km long, and 0.15 to 0.35 km wide. F1

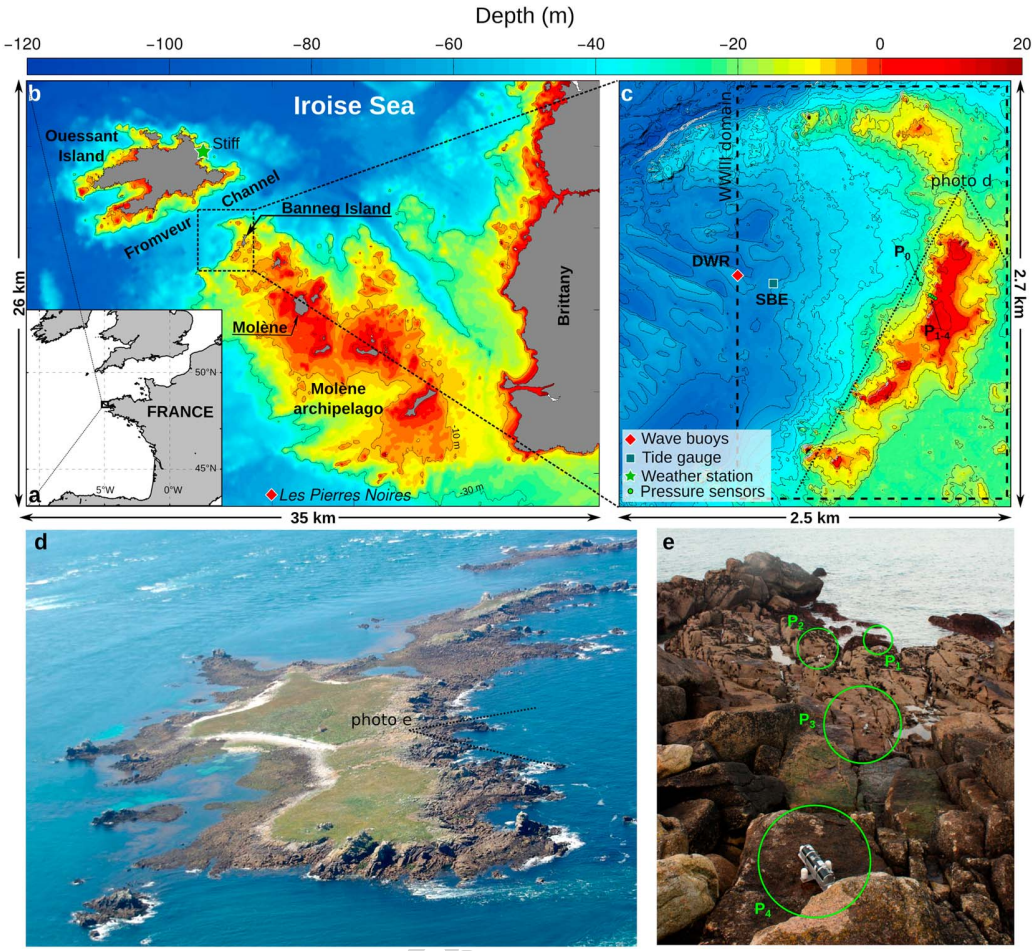

Figure 1. (a) Location of the Molène archipelago. (b) Bathymetry of the Molène archipelago and location of Banneg Island. (c) Topography and bathymetry of Banneg Island (isolines are given every 5 m) and model domain. (d) Aerial photograph of Banneg Island showing the location of the instrumented cross-shore profile. (e) Photograph of the four pressure sensors taken from the top of the cross-shore profile. DWR = Datawell DWR-MkIII; SBE = Seabird Electronics SBE26+.

The western coast is cut into steep cliffs ($\tan\beta > 0.5$) that include a series of high headlands (16 to 20 m above mean sea level [MSL]) and lower cliffs (12 to 13 m above MSL) with more gentle slopes ($0.15 < \tan\beta < 0.4$) in embayments. These cliffs present an orthogonal tabular structure resulting from the horizontal bedding and nearly vertical joint system affecting the granite bedrock. Erosive processes have carved the cliffs by quarrying rocks from the bedrocks and the remaining sockets contribute to the rugged morphology of the western part of the island (Figure 1d).

This region is characterized by a semidiurnal macrotidal regime with tidal ranges from 2 to 8 m in neap and spring tide conditions, respectively (SHOM, 2014). The area around Ouessant Island is likely the part of the French coastline most exposed to waves. The wave buoy *Les Pierres Noires* (5.0° W ; 48.2° N ; 60-m depth, WMO number 62069) recorded significant wave height (H_s) larger than 12 m (e.g., during Ruzica storm on 8 February 2015) and winter-averaged H_s varied between 2.1 and 3.7 m, from 2008 to 2016. On Banneg's shores, waves are attenuated by the sheltering effect of Ouessant Island. The results of a 14-year (1993–2013) high-resolution regional wave hindcast (Boudière et al., 2013; Roland & Ardhuin, 2014) indicate that the winter-averaged H_s, peak period (T_p), and mean wave direction (θ_m), 1 km west of Banneg Island, are 1.8 m, 11.8 s, and 242.9°, respectively. During this period, the simulated H_s never exceeded 7 m. Ardhuin et al. (2012) also showed that the tidal currents in the Fromveur Channel have a strong influence on the propagation of incident waves due to current-induced wave refraction and dissipation and the blocking of high-frequency waves in opposite currents.

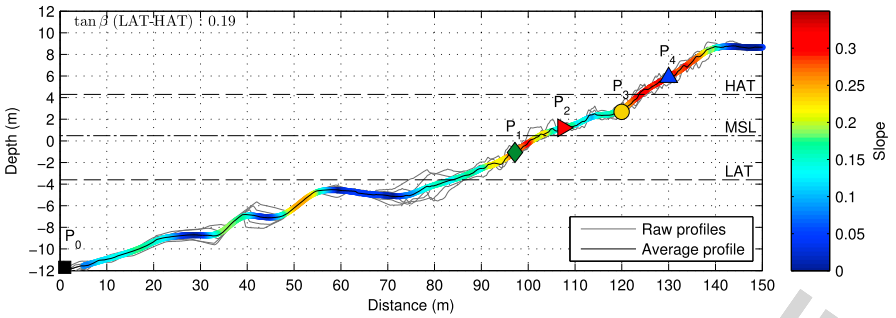

Figure 2. Depth along the instrumented cross-shore profile and positions of the pressure sensors. The gray lines correspond to 2-m spaced parallel profiles used to compute the average profile (black line). The thick colored line indicates the slope value of a smooth profile computed with a 10-m-wide sliding window. HAT = highest astronomical tide level; MSL = mean sea level; LAT = lowest astronomical tide level.

For more than two decades, Banneg Island has been investigated by geomorphologists, who put in evidence the strong morphogenic impacts of storm waves on the island (Fichaut & Hallégouët, 1989; Fichaut & Suanez, 2011). Indeed, more than 1,000 m^3 of cliff-top storm deposits, with weight of a single piece up to 30 tons, were quarried from the cliff-top and accumulated at the rear of the embayments. The furthest accumulation lies 100-m inland (Suanez et al., 2009). Autret et al. (2016) carried out a detailed analysis of cliff-top storm deposits trajectories from prestorm and poststorm drone-based surveys. They related these trajectories to synchronous underwater pressure measurements in order to detect the morphogenic overwashing events that occurred during the 2013–2014 winter. They also estimated possible runup values from an empirical formula and found runup extremes above 15 m in parts of the island. However, in the absence of runup measurements, these guesses rely on the extrapolation of the runup formula proposed by Stockdon et al. (2006) for beaches. Another study on the Banneg cliff hydrodynamics used data from the 2008–2009 winter and focused on infragravity waves which were found to be exceptionally high (Sheremet et al., 2014) and are expected to form a significant fraction of the runup. Here we use more recent and more extensive data to provide runup measurements and explore the physical processes that control wave runup over steep rocky cliff.

2.2. Field Survey

From October 2012 to May 2015, three extensive field surveys were carried out at Banneg Island in order to characterize offshore and nearshore hydrodynamics in stormy conditions. During each winter, a directional waverider (Datawell DWR-MkIII, hereafter referred to as DWR) and a bottom-mounted pressure sensor (Seabird Electronics SBE26+, hereafter referred to as SBE) were deployed 1-km offshore west of Banneg Island, in approximately 50-m water depth (Figure 1c), providing information on the incident wave field and water levels. In addition, four pressure sensors (Ocean Sensor System, OSSI-010-003C) were installed along a cross-shore profile, within an embayment of the western part of the island (Figures 1d and 1e). These sensors were evenly spaced (~10 m) from the bottom to the top the cliff so that they could record swash event at every possible tidal stage and over varying foreshore slopes. The lowest sensor was located 2.5 m above the lowest astronomical tide level (LAT) and the highest sensor was located 1.60 m above the highest astronomical tide level (HAT). Each OSSI sensor was held in a stainless steel mount affixed to the bedrock with threaded rod. The sensor heads were protected by perforated steel plates to prevent membrane damage and damp the dynamical pressure effect. The sensor's height above the bed was approximately 12 cm. Hereafter, these pressure sensors will be named P_1, P_2, P_3, and P_4, from the bottom to the top of the cliff (Figure 2). Finally, during the 2012–2013 winter, one additional pressure sensor was deployed 100-m seaward of the instrumented cross-shore profile, in 12-m water depth. This sensor, named P_0 in the following, recorded one 20-min pressure burst per day and was only used to validate the results of a wave model. Note that SBE was lost during the 2012–2013 winter campaign, and P_2 OSSI sensor was crushed by a boulder during the 2013–2014 winter campaign, resulting in missing data.

3. Methods

3.1. Observed Offshore Parameters

Offshore water levels were estimated from the SBE tide gauge. After correcting the raw pressure for the atmospheric pressure (measured at the Stiff weather station on Ouessant Island, see Figure 1b) and converting

this pressure into water elevation assuming hydrostatic equilibrium, the mean value was subtracted from the corrected time series in order to reference the water elevation with respect to MSL. For consistency with bathymetric and topographic information, all hydrodynamic observations were then referred to the IGN69 topographic French datum. For the 2012–2013 winter, since no measurements were available at the SBE tide gauge, we used outputs from the circulation model MARS (Ardhuin et al., 2012; Lazure & Dumas, 2008) at the same location. The observed water levels were very well reproduced by the model, with a root-mean-squared error of 0.08 m and a squared correlation coefficient (ρ^2) of 0.99.

Offshore wave parameters were estimated from the directional spectra measured by the DWR. Runup statistics are usually parameterized in terms of peak period T_p. It will be demonstrated that, in our context, better regressions are obtained using integrated mean wave periods, which are more likely to account for the spectral shape, as observed by Poate et al. (2016). The significant wave height and the wave periods $T_{m0,1}$, $T_{m0,2}$, $T_{m0,-1}$, and $T_{m0,-2}$ were computed from the spectral moments

$$m_p = \int_0^{f\max} f^p E(f)\mathrm{d}f, \tag{2}$$

with

$$H_s = 4\sqrt{m_0}, \tag{3}$$

and

$$T_{m0,p} = \left(\frac{m_p}{m_0}\right)^{-1/p} = \left(\frac{\int_0^{f_{\max}} f^p E(f)\mathrm{d}f}{\int_0^{f_{\max}} E(f)\mathrm{d}f}\right)^{-1/p}, \tag{4}$$

where $f_{\max}$ is a cut-off frequency. The mean wave direction θ_m (given hereafter in meteorological convention) was computed as

$$\begin{aligned} \theta_m &= \arctan\left(\frac{b}{a}\right), \\ a &= \int_0^{2\pi}\int_0^{f\max} \cos(\theta)E(f,\theta)\mathrm{d}f\mathrm{d}\theta, \\ b &= \int_0^{2\pi}\int_0^{f\max} \sin(\theta)E(f,\theta)\mathrm{d}f\mathrm{d}\theta. \end{aligned} \tag{5}$$

The peak period was computed from the spectral maximum at the peak frequency f_p, as $T_p = 1/f_p$.

3.2. Simulated Nearshore Parameters

Given the complex bathymetric and hydrodynamic settings of Banneg Island, offshore wave measurements are not necessarily representative of the wave conditions that reach Banneg's shores. The wave conditions at the bottom of the cliff could be provided by submerged sensors, but only at high tide. Therefore, we propagated the offshore wave conditions to the nearshore using a phase-averaged wave model. We used the spectral wave model WAVEWATCH III® (WWIII, V6.10, Tolman, 2014), implemented on a rectilinear computational grid with a constant along-shore 10-m resolution and a cross-shore resolution refined from 10 m at the west boundary to 1 m at the shore (Figure 1c). In order to decrease the computational cost, we used the new fully implicit version of WWIII based on the work of Roland (2009). This new version of WWIII solves all propagation dimensions and integrates the source terms without any splitting, based on Patankar rules. This fully implicit version model was already used and validated in various studies (Hesser et al., 2018; Leckler et al., 2016; Smith et al., 2017). The model was forced with directional spectra measured by the DWR and with water levels and currents simulated by the MARS model implemented on the Iroise Sea at a resolution of 250 m (Ardhuin et al., 2012; Pineau-Guillou et al., 2014). Deep-water source terms have little impact on this scale, and we used parameterizations by Ardhuin et al. (2010) and Hasselmann and Hasselmann (1985). Shallow water effects included here are the nonlinear triad interactions computed using the LTA parameterization by Eldeberky et al. (1996) and depth-induced breaking as parameterized by Battjes and Janssen (1978), with the dissipation constant α set to 1 and the breaking threshold γ set to 0.73.

We validated the model results against pressure records at P_0 in 12-m water depth. For each 20-min records, pressure spectra were computed on 50% overlapped segments of 1,024 samples, detrended and tapered

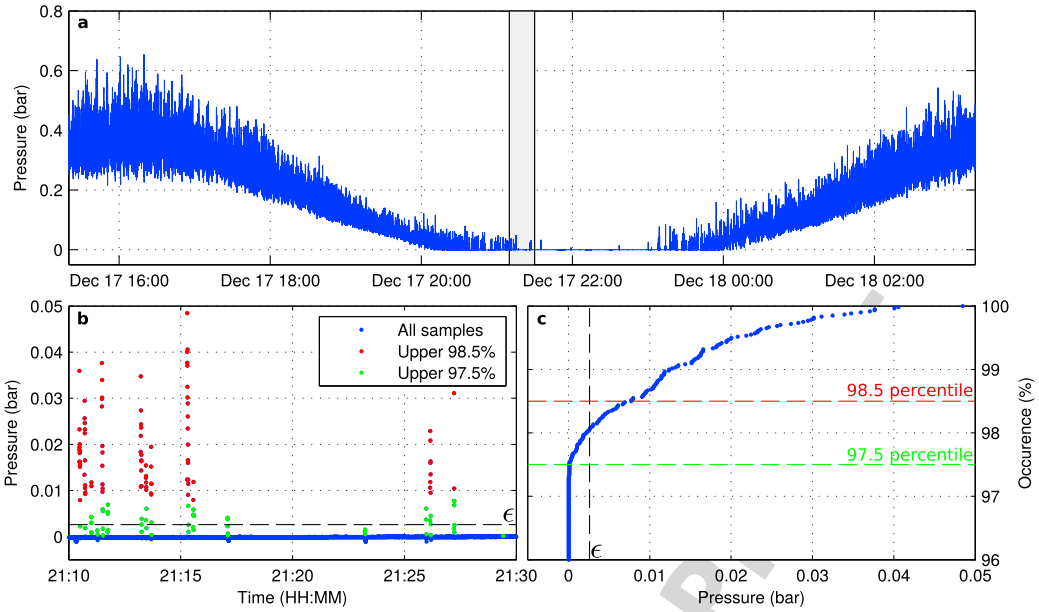

Figure 3. (a) A 12-hr time series of pressure measurements, during which one η_2 value was computed, (b) 20-min burst of pressure data (shown in gray in a) during which the 98.5 (97.5) percentile was higher (lower) than ϵ (black-dashed line), and (c) cumulative distribution of the 20-min pressure data showing the intersection between the data and ϵ occuring within the 98.5 and 97.5 percentiles. η_2 is then computed as the difference between the sensor elevation and the still water level measured during this period.

with a Hanning window to suppress tidal motions, and reduced spectral leakage. The resulting spectra had a spectral resolution of 0.005 Hz, a bandwidth of 2.49 Hz (0.01 – 2.5 Hz), and 12 degrees of freedom. The pressure Fourier coefficients were then converted into sea surface elevation spectra based on linear wave theory. Finally, the significant wave height was computed from equation (3), using a cut-off frequency $f_{max} = 0.25$ Hz, above which the signal became dominated by noise.

The model showed excellent skills for reproducing H_s, with a bias of 0.03 m, a normalized root-mean-square error of 12.4%, and a squared correlation coefficient of 0.94. Therefore, simulations were run for each of the detected runup events (see sections 3.3 and 4.2), and H_s outputs at P_0 were then reverse shoaled to deep water using linear wave theory. The resulting equivalent offshore significant wave height, named H_0, was used in the regression analysis presented hereafter.

3.3. Estimation of the 2% Exceedance Level of Shoreline Elevation η_2

The pressure time series measured in the swash zone were analyzed to infer an extreme value statistical parameter for wave runup. By contrast to studies in smooth bottom and mild slope context, the bottom pressure measurements are expected to be significantly affected by nonhydrostatic effects due to high-velocity flow. Ad hoc alternative approaches have been used here to avoid taking into account the effect of dynamical pressure, based on level detection thresholds rather than magnitude of the bottom pressure. Once the atmospheric pressure is subtracted from the raw signal, swash bores appear as individual spikes separated by longer intervals of near-zero pressure when the sensor is dry (Figure 3). Our method consisted in finding the 20-min time periods, during which the sensor was immersed 2% of the time only. Then, the extreme wave runup parameter was computed as the difference between the elevation of the sensor and the still water level (SWL), computed as the offshore water level averaged over this 20-min time window. Note that SWL is a time-varying reference level that includes the tidal signal and the atmospheric surge. This runup elevation corresponds to the 2% exceedance level of shoreline elevation, as defined by Holman (1986). These authors named this parameter η_2, to distinguish it from R_2, which is computed from the distribution of individual maxima of shoreline elevation. The variable name η_2 will also be adopted in this study. Because of the inherent accuracy and resolution of the instruments and the uncertainty on the local atmospheric pressure (the weather station used to correct the data was located 5 km away), the pressure measured by the sensors when

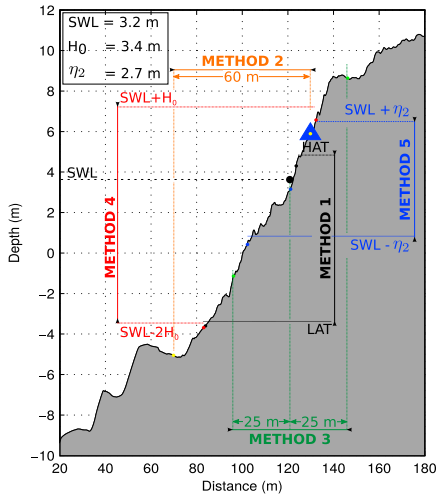

Figure 4. Sketch of the profile showing the different regions used to compute the slopes for each method tested in this study. The hydrodynamic conditions corresponding to this example are given in the top left inset. The blue triangle corresponds to the position of sensor P_4. Note that our pressure-sensor-based method to compute η_2 imposes that $SWL + \eta_2$ is always equal to the elevation of the sensor, with respect to SWL. SWL = still water level; HAT = highest astronomical tide level; LAT = lowest astronomical tide level.

they were dry was not strictly equal to zero but noisy and slightly biased. η_2 estimates were thus obtained when the 20-min time periods, during which the 1.5% and 2.5% exceedance levels were, respectively, higher and lower than a threshold value ϵ. This threshold value was obtained by computing the means ($\overline{p_0}$) and the standard deviation (σ) of a large amount of 20-min bursts, measured when the sensors were dry and using the maximum values as follows:

$$\epsilon = \overline{p}_{0,\max} + 2\sigma_{\max}. \quad (6)$$

Assuming a Gaussian distribution of the noise, using $2\sigma_{\max}$ ensured our threshold to be higher than 95.4% of the dry samples. Figure 3 illustrates the methodology applied to a 20-min sample of pressure measurements in the swash zone.

It is important to note that with our method, runup measurements were collected at discrete times and specific locations, only when the sensors were in the swash zone. Hence, our method could not capture wave runups that exceed the sensor's position and was therefore not adequate to record the most extreme events. However, with four sensors deployed along a transect recording over a sufficiently long record period, robust information on extreme runup values (in a statistical sense) were obtained for a large range of wave and tidal conditions. Moreover, as explained previously, inferring runup statistics from η_2 estimates allows to directly process the pressure data without the need to reconstruct free surface elevation through hydrostatic assumption and thus make it possible to ignore dynamic pressure effect.

3.4. Definition of the Foreshore Slopes

Many studies showed that the wave runup is dependent on the foreshore slope, whether from laboratory experiments (Blenkinsopp et al., 2016; Hunt, 1959; Van der Meer & Stam, 1992), or field data (Holman, 1986; Stockdon et al., 2006; Suanez et al., 2015; Poate et al., 2016). For this latter case, several methods were proposed to compute the slopes on irregular profiles and/or macrotidal environments. Holman (1986) computed the foreshore slope as the average slope over a 5-m-long segment surrounding the MSL. Stockdon et al. (2006) defined the foreshore slope as the average slope over a region $\pm 2\sigma$ around $< \eta >$, with σ the standard deviation of the continuous shoreline elevation and $< \eta >$ the average shoreline elevation (i.e., the SWL plus the wave setup). Other authors used the offshore significant wave height as a proxy for the swash zone extent and computed the foreshore slope on a time-varying section varying with the tide and the wave conditions, but different fraction of H_0 are used in different studies (Poate et al., 2016; Suanez et al., 2015). For instance, Suanez et al. (2015) used $SWL \pm 0.25H_0$ to compute the upper and lower bounds of the profile section, while Poate et al. (2016) used $SWL + H_0$ to compute the upper bound and $SWL - 2H_0$ to compute the lower bound. These field studies were mostly conducted on sandy coasts, characterized by relatively smooth topographic gradients. On rocky coasts exposed to waves, such as the western coast of Banneg Island, the slope is very irregular, and the different estimates can give very different values. Several methods to compute the cliff slopes were thus tested in this study. The bathymetric and topographic data were retrieved from a high-resolution digital elevation model, continuous at the land-sea interface, acquired with airborne lidar and vessel-mounted multibeam sounders (Litto3D; ; Louvart & Grateau, 2005). A 150-m-long profile intersecting the pressure sensors' location was interpolated at 0.5-m resolution, and four additional 2-m-spaced parallel profiles were used to compute an average profile with the small-scale features removed (Figure 2). Then, the foreshore slopes were computed with a linear regression fitted through the cliff profiles over a region dependent on the selected method. Five methods (Figure 4) were defined and are listed below in increasing order of complexity:

- For the first method (M_1), we considered a segment vertically bounded between LAT and HAT. This method provided slopes that do not vary with time, identical for the four sensors of the profile, and was used as a baseline to compare with the four following method;
- For the second method (M_2), we considered a 60-m-long segment right bounded by the profile intersection with the instrument's position, which always corresponds to $SWL + \eta_2$. This method provided stationary slopes, dependent on the sensor's location only;

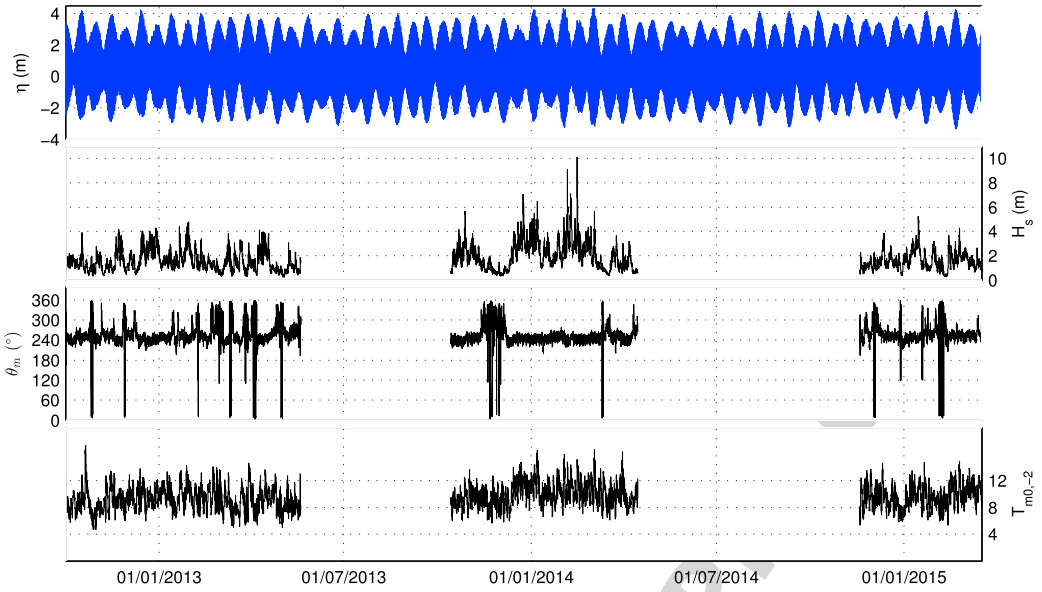

Figure 5. From top to bottom, time series of offshore significant wave height, water level, mean wave period $T_{m0,-2}$, and mean wave direction from October 2012 to March 2015. In the first panel, the blue line shows the MARS outputs when no tide measurements were available.

- For the third method (M_3), we considered a 50-m-long segment horizontally centered on the intersection between *SWL* and the profile. This method provided time-varying slopes, dependent on the tide, but independent of the wave conditions, similar (except for the chosen length) to the one of Holman (1986);
- For the fourth method (M_4), we considered a segment vertically bounded by $SWL + H_0$, for the upper bound, and $SWL - 2H_0$, for the lower bound. This method provided wave- and tide-dependent slopes, similar to the one used by Poate et al. (2016);
- For the fifth method (M_5), we considered a segment vertically bounded by $SWL \pm \eta_2$. This method provided runup- and tide-dependent slopes, computed over a segment that approximated the swash zone extent, as in Stockdon et al. (2006).

In methods M_2 and M_3, several segment lengths were tested iteratively, and our selection (60 and 50 m, respectively) was based on the results described in section 4.3.2.

4. Results

4.1. Offshore Water Levels and Wave Conditions

Offshore water levels recorded by SBE and mean wave parameters recorded by DWR between October 2012 and April 2015 are shown on Figure 5. The tidal range was comprised between 1.7 and 7.4 m and was 4.4 m on average. The mean H_s was 1.7 m. During the 2013–2014 winter, several storms generated H_s larger than 6 m, with a maximum of 10 m on February 14. During this winter, the mean H_s was 2.1 m. According to Masselink et al. (2016), the 2013–2014 winter had the highest winter-mean wave heights along the Atlantic coast of Europe since at least 1948. Our measurements are consistent with this finding when we compare them to the long-term wave hindcast of Boudière et al. (2013), who found a maximum H_s of 7 m and a winter mean H_s of 1.8 m at the same location, for the period 1993–2014. The mean wave period $T_{m0,-2}$ was 9.5 s on average and reached up to 17.5 s. The mean wave direction (θ_m) was 253° on average. Periods of calm wave conditions were usually associated with short period waves of NE directions, indicating that anticyclonic conditions prevailed.

4.2. Wave Transformation in the Nearshore

Wave dynamics around Banneg Island is strongly affected by the complex bathymetric and hydrodynamic settings of the Molène archipelago. Ardhuin et al. (2012) described the large-scale effect of tidal currents in the Molène archipelago on the incoming wave field. Their model results revealed a strong focusing of the wave energy toward the Fromveur ebb tidal jet and high wave dissipation rates in the center of the jet. In the present study, the wave data recorded simultaneously at DWR and P_0 during winter 2012–2013, and the high-resolution wave model implemented in the Banneg area provides some details on the wave transfor-

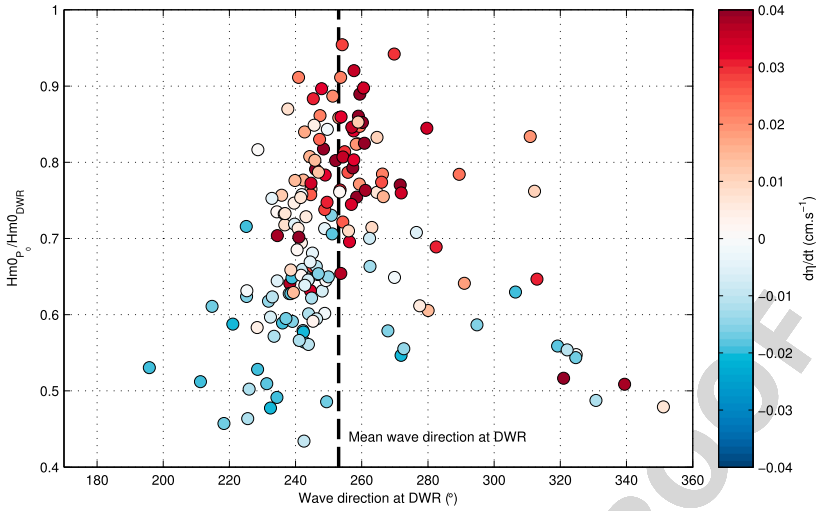

Figure 6. Scatter diagram of the ratio $Hm0_{P0}/Hm0_{DWR}$ versus the wave direction measured at *DWR*. The color scale represents the gradient of elevation and indicates the tidal stage (red for flood and blue for ebb).The black-dashed line indicates the average mean wave direction at DWR. DWR = Datawell DWR-MkIII.

mation in the nearshore zone of Banneg Island. First, the combined effects of bathymetry and tidal currents on the wave energy between DWR and P_0 are illustrated in Figure 6, which depicts the ratio of H_s measured by P_0 to H_s measured by DWR versus the wave direction measured by DWR. The color code corresponds to the time derivative of tidal elevation measured at SBE, used here as a proxy for the tidal stage. One notes first the significant role played by the tidal phase on the wave direction at DWR. The main trend is that flood (ebb) currents are generally associated with more southern (northern) wave direction, which is a local illustration of the tidal jet refraction effect described by Ardhuin et al. (2012). The role of local refraction between the incoming wave field at DWR and the input point of our surveyed site P_0 is quantified by wave heights ratio versus wave direction in Figure 6. The refraction effect is clear: the transmission of wave energy from DWR to P_0 is maximal for wave direction between 250° and 260°, which is around the mean wave direction at DWR, and significantly decreases when departing from such optimal incidence angle. The spectral transformation of the wave energy between DWR and P_0 is illustrated by Figure 7, which shows the mean spectrum at DWR and P_0, averaged over the 167 daily events recorded by P_0. We can see a significant attenuation of the wave energy from DWR to P_0 as well as a transfer of energy toward lower frequencies at P_0. This spectral evolution likely results from current-induced enhanced energy dissipation, current and bathymetric refraction, and nonlinear energy transfer. Finally, the impact of the complex nearshore bathymetry on the incident wave field at Banneg Island is illustrated by Figure 8, which shows a typical wave field reaching the west coast of Banneg, simulated with WWIII. One notes the strong effect of bathymetric refraction, which induces alongshore modulations of wave height and changes in wave direction. The surveyed area is located in a wave divergence area, where wave height is nearly halved compared to the values simulated 200-m southward. In addition, it is expected that the complex roughness structure of the rocky bed plays a role on the incoming wave transformation by increasing dissipation from the shoaling zone, which is out of the scope of the present study dedicated to runup processes. These observations highlight the complexity of the wave propagation at the Banneg's shore and further justify the need to use reverse-shoaled wave height at P_0, as a relevant input wave forcing to study subsequent runup processes. Note that the ratio H_s to local depth at P_0 is lower than 0.25 80% of the time and never exceeds 0.48, which indicates that depth-limited wave breaking offshore of P_0 may occur only very occasionally.

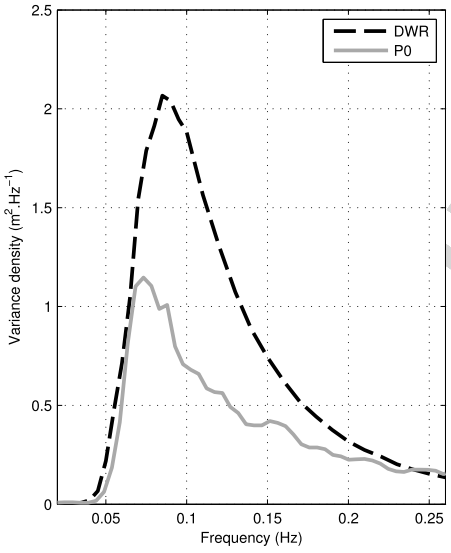

Figure 7. Wave energy spectra at DWR (black-dashed line) and P_0 (solid gray line) average over 167 events, corresponding to all the available daily records at P_0. DWR = Datawell DWR-MkIII.

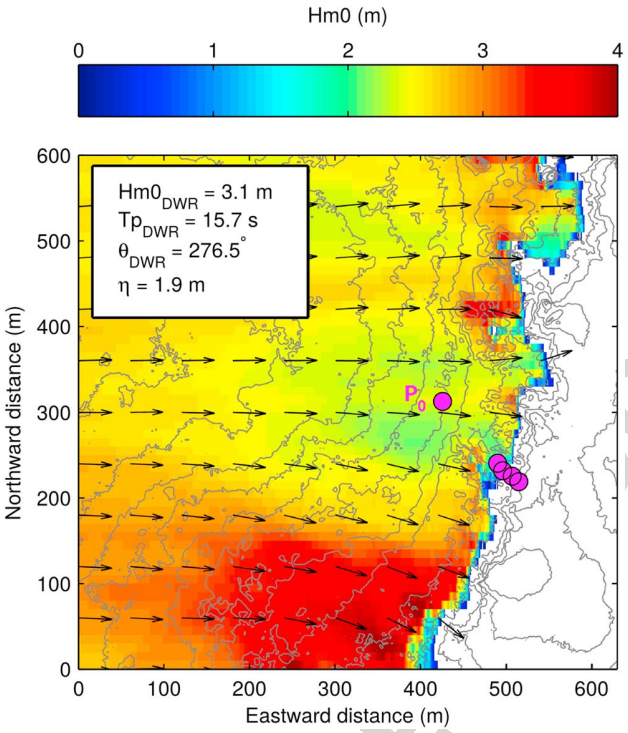

Figure 8. Field of significant wave heights in the nearshore zone simulated with the model WAVEWATCH III. The magenta circles show the locations of the sensors. The isodepth lines are given every 3 m. DWR = Datawell DWR-MkIII.

4.3. Wave Runup

Between October 2012 and March 2015, 739 runup values were computed (Table 1). The largest number of η_2 values was obtained at sensor P_2 (376), followed by P_3 (143) although no data were available at this sensor during the 2013–2014 winter. In comparison, fewer η_2 values were obtained at P_1 (122) and P_4 (131), likely because these sensors were less often in the swash zone, due to their position slightly above the LAT (for P_1) and above the HAT (for P_4).

Figure 9 shows the distribution of η_2 values obtained at each sensor against the associated offshore water levels and significant wave heights. As a consequence of our methodology, the altitude of the sensor constrained the range of hydrodynamic conditions associated with the observed runup values. For instance, P_1, located at the bottom of the profile, measured η_2 at low tide for H_s of 1.1 m on average, while P_4, located at the top of the profile, measured η_2 at high tide for H_s of 2.6 m on average. All in all, owing to the long time period covered by the measurements, the full tidal range and wave heights comprised between 0.2 and 4.7 m were encompassed in our η_2 measurements.

4.3.1. Wave Runup Dependence on Offshore Wave Parameters

The dependence of wave runup on offshore wave parameters was assessed through a correlation analysis. Seven parameters were tested: the offshore significant wave height H_0, the peak period T_p, the spectral peri-

Table 1
Number of Runup Events Detected for Each Sensors and Associated Mean Offshore Significant Wave Height, Mean Water Level, and Mean, Minimum, and Maximum η_2

	# of events	Mean water level (m)	$\overline{H_s}$ (m)	$\overline{\eta_2}$ (m)	$\eta_{2,min}$ (m)	$\eta_{2,max}$ (m)
P_4	131	2.9	1.1	3.0	2.0	5.3
P_3	143	1.3	1.6	1.3	0.2	3.4
P_2	376	0.1	1.3	1.1	0.1	4.1
P_1	122	−1.7	2.6	0.6	0.04	2.0

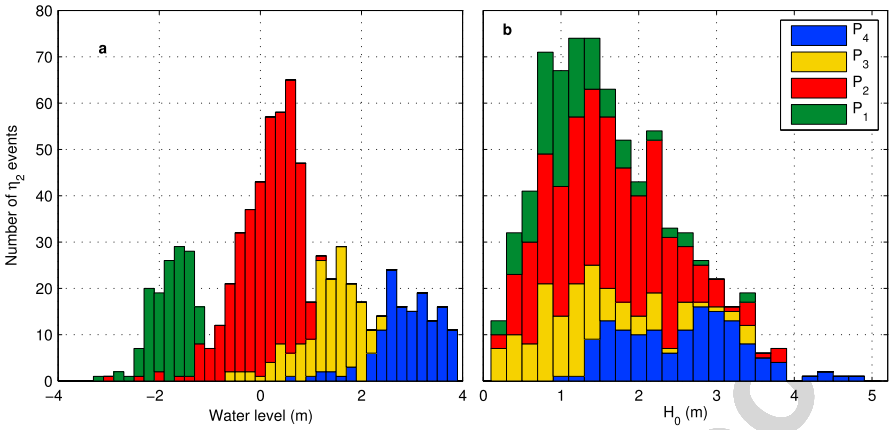

Figure 9. Histograms of the number of η_2 events detected by each sensor against the offshore water level (a) and the significant wave height (b).

ods $T_{m0,1}$, $T_{m0,2}$, $T_{m0,-1}$, and $T_{m0,-2}$, and the ratio of H_0 to the wave steepness $\sqrt{H_0/L_0}$, which is equal to $\sqrt{H_0L_0}$. This last parameter appears in the dimensional form of equation (1). Although some authors presented their results in nondimensional space, we performed our analysis with dimensional parameters in order to reduce the errors associated to small wave cases, as explained by Stockdon et al. (2006). Indeed, the data in nondimensional space were much more scattered than in dimensional space, and the least-square coefficients differed from one approach to the other. The results of the correlation analysis are given in Table 2, and the scatter diagrams for H_0 and $\sqrt{H_0L_0}$ are shown on Figure 10.

For H_0, the squared correlation coefficients ranged between 0.58 (P_1) and 0.83 (P_3), with an average of 0.71, indicating a good fit between η_2 and H_0 (Figure 10a). For the wave periods, ρ^2 was comprised between 0.22 and 0.61, indicating a lower dependency between η_2 and the wave period. Although the highest individual scores depended on which sensor was considered, the sensor-averaged scores revealed that T_p was the parameter that worst correlated with runup, which is due to the fact that peak periods are usually fairly noisy (Young et al., 1995) and that the wave energy at frequencies higher than the peak frequency also contributes to the wave runup. The importance of wave periods is better investigated using mean periods, with slightly higher correlation using $T_{m0,1}$ or $T_{m0,2}$. Both the wave height and wave periods are important factors determining the runup, and their combination in a Hunt-like parameter (Hunt, 1959) $\sqrt{H_0L_0}$ gives a very good predictor of runup, in particular when L_0 is defined from $T_{m0,-2}$ as $L_0 = gT_{m0,-2}^2/(2\pi)$ using linear wave theory. The slightly better fit using $T_{m0,-2}$ instead of $T_{m0,-1}$ comes from a dominant effect of long period swells also found by Ardhuin et al. (2014) for the estimation of infragravity wave heights. This parameter $\sqrt{H_0L_0}$ was retained for the following analysis. The correlations between η_2 and $\sqrt{H_0L_0}$ (Figure 10c) were very high ($\overline{\rho^2} = 0.80$) and confirmed the linear relationship existing between these parameters, already demonstrated for different environments (e.g., Holman, 1986; Hunt, 1959; Stockdon et al., 2006; Suanez et al., 2015). Note also that T_p will be used here only for comparison with previous work (Holman, 1986), while the more relevant $T_{m0,2}$ will be kept for the remaining analysis.

Our data set confirms the existence of a linear relationship between η_2 and $\sqrt{H_0L_0}$ for each individual sensor. However, the slopes of the regression lines between η_2 and $\sqrt{H_0L_0}$ (dashed lines in Figure 10b) vary from

Table 2
Squared Correlation Coefficients (ρ^2) Between η_2 and Offshore Wave Parameters

	H_0	T_p	$T_{m0,1}$	$T_{m0,2}$	$T_{m0,-1}$	$T_{m0,-2}$	$\sqrt{H_0L_0}$
P_4	0.78	0.41	0.61	0.61	0.60	0.59	0.88
P_3	0.83	0.27	0.54	0.56	0.51	0.49	0.88
P_2	0.64	0.22	0.36	0.37	0.35	0.35	0.74
P_1	0.58	0.23	0.40	0.40	0.38	0.37	0.68
Mean	0.71	0.28	0.48	0.48	0.46	0.45	0.80

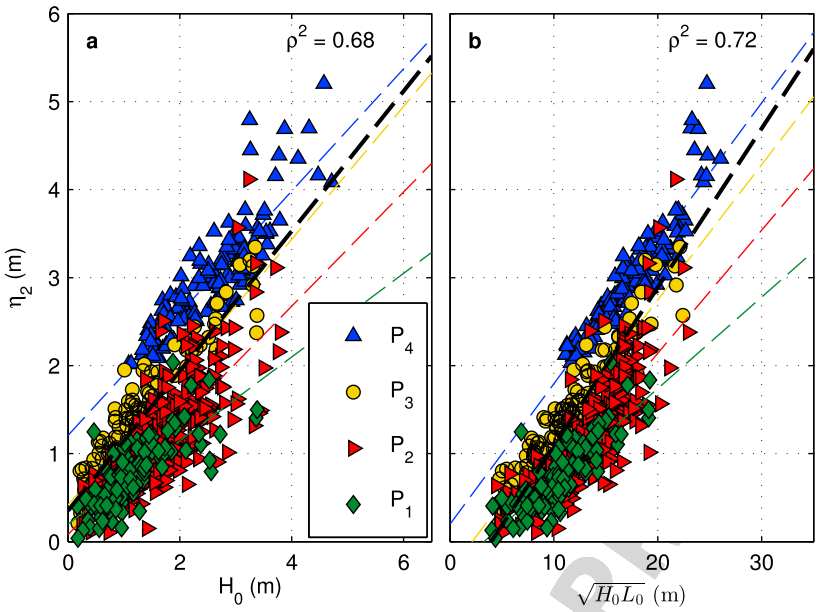

Figure 10. Scatter diagrams of η_2 versus H_0 (a) and η_2 versus $\sqrt{H_0L_0}$ (b). Regression lines are indicated with colored-dashed lines for each instrument and with a black-dashed line for the full data set. The squared correlation coefficients computed for the whole data set are indicated on the top right hand corner.

sensor to sensor: 0.07 for P_1, 0.10 for P_2, 0.11 for P_3, and 0.12 for P_4. These differences likely traduced the impact of the local morphology on the wave runup.

4.3.2. Wave Runup Dependence on the Foreshore Slopes

The impact of the morphology was quantified by introducing a measure of the foreshore slopes in the runup formula. We now look at correlations between η_2 and $\tan\beta\sqrt{H_0L_0}$. For each runup event detected by the pressure sensors, the slope was computed with each of the five methods defined in section 3, and time series of $\tan\beta\sqrt{H_0L_0}$ were generated. Figure 11 shows the scatter diagrams of η_2 against $\tan\beta\sqrt{H_0L_0}$ with $\tan\beta$ computed with these five methods, and Figure 12 shows the mean and the range of the slope values computed with the five methods (left-hand panel), as well as the length of the segment over which the slopes were computed (right-hand panel).

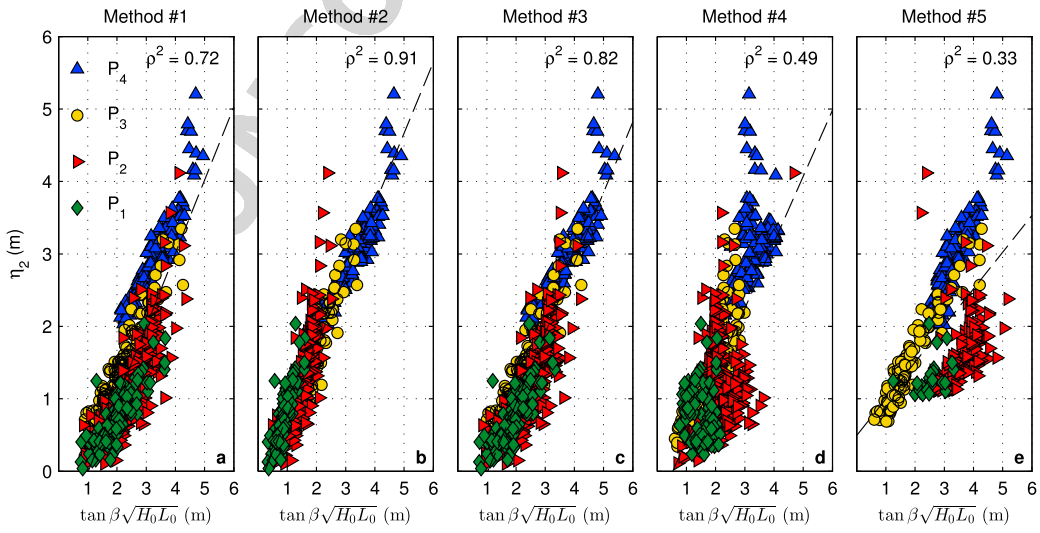

Figure 11. Scatter diagrams of η_2 versus $\tan\beta\sqrt{H_0L_0}$, with $\tan\beta$ the forshore slope computed with method 1 to 5 (a–e). The squared correlation coefficients computed for the whole data set are indicated on the top right hand corner.

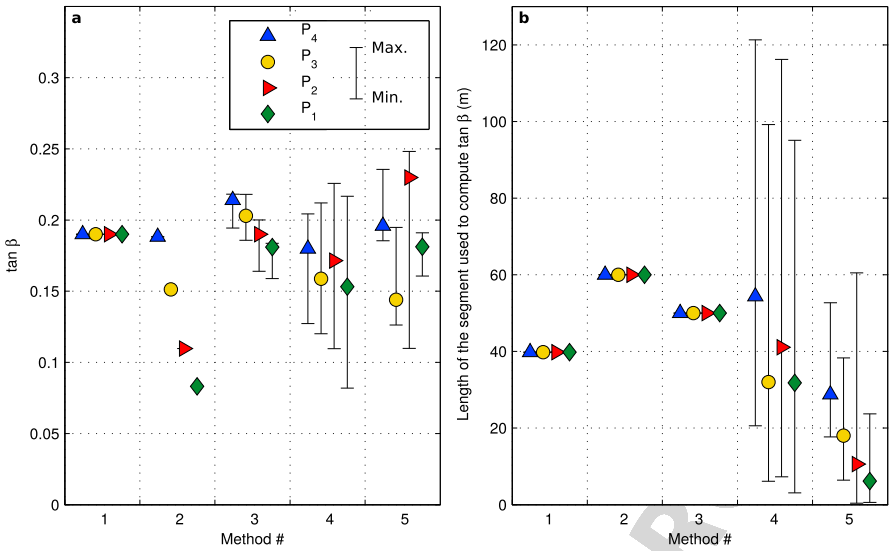

Figure 12. Slopes (a) and length of the segment used to compute the slopes (b) at each sensor for the five methods. The colored symbols indicate the mean value, and the vertical bars indicate the minimum and maximum values.

The slopes computed with method M_1 were constant in time and identical for all sensors of the profile ($\tan\beta = 0.19$). This method was used as a baseline method, against which the four other methods were compared to. With this method, the squared correlation coefficient between η_2 and $\tan\beta\sqrt{H_0L_0}$ was $\rho^2 = 0.64$. The slopes computed with method M_2 only depended on the sensors location and decreased from P_4 ($\tan\beta = 0.20$) to P_1 ($\tan\beta = 0.08$). This method improved the correlations, with a squared correlation coefficient ($\rho^2 = 0.91$) 42% larger than the one obtained with the baseline method M_1. The mean slopes computed with method M_3 were comprised between 0.18 (P_1) and 0.21 (P_4), and the slope ranges did not exceed 0.04. This method improved the correlations, with a squared correlation coefficient ($\rho^2 = 0.76$) 19% larger than the one obtained with M_1. The mean slopes computed with method M_4 were comprised between 0.16 (P_1) and 0.18 (P_4), and the slopes ranges were larger (up to 0.17) with this method than with M_3. The squared correlation coefficient associated to this fourth method ($\rho^2 = 0.49$) was 23% lower than the one obtained with M_1. Finally, the mean slopes computed with method M_5 were comprised between 0.14 (P_3) and 0.28 (P_1), and the slope ranges reached up to 0.47 at P_2. The associated squared correlation coefficient ($\rho^2 = 0.34$) was 47% lower than the one obtained with M_1. These results clearly showed that the method used to compute the slopes was critical when assessing the impact of the cliff slope on the wave runup. While methods M_2 and M_3 provided evidence that the runup values could be related to the slopes of the profile, method M_4 and M_5 tended to show the opposite. These differences were mostly attributed to the varying lengths of the segments over which the slopes were computed, depending on the selected method (Figure 12b). The general trend, which will be further discussed in the next section, is that methods involving a wide part of the foreshore in the slope calculation (M1, M2, and M3) show more consistent regressions than forcing-dependent methods (M4 and M5), which promote the effect of local topography, resulting in increased variability.

5. Discussion

Despite some limitations inherent to our study site and our methodology, further discussed below, our study revealed important features of wave runup in rocky cliff environments. First, the wave runup η_2 is mostly associated to significant wave heights that explain 68% of the variance. Because the wave periods have a lower variability, they explain only 13% of the variance, but the combination of height and period in $\sqrt{H_0L_0}$ (Hunt, 1959) explains more than 70% of the runup variance in our data set (Figure 10b).

Following Stockdon et al. (2006), wave heights reverse shoaled to deep water are preferable over deep water wave measurements that are not always representative of nearshore conditions. In the case of Banneg Island, where the highly irregular nearshore bathymetry and the currents of the Fromveur Channel strongly impacts

Table 3
Squared Correlation Coefficients Between η_2 and H_0, $T_{m0,2}$, $T_{m0,-2}$, and $\sqrt{H_0 L_0}$ Measured at DWR and P_1 and Simulated at P_0

	H_0			$T_{m0,2}$			$T_{m0,-2}$			$\sqrt{H_0 L_0}$		
	DWR	P_0	P_1	DWR	P_0	P_1	DWR	P_0	P_1	DWR	P_0	P_1
P_4	0.75	0.78	**0.79**	**0.61**	0.33	0.49	0.59	0.47	**0.80**	**0.87**	0.86	0.86
P_3	0.77	0.83	**0.89**	**0.56**	0.16	0.46	0.49	0.22	**0.65**	**0.87**	0.87	0.75

Note. The bold font indicates the best score within the three estimates of the parameter. DWR = Datawell DWR-MkIII.

the wave propagation, this issue was particularly relevant. We compared η_2 with H_0 from three different locations: (1) in deep water, as measured by DWR; (2) in intermediate water, as simulated by WW3 at P_0 and reverse shoaled to deep water; and (3) in shallow water, as measured by P_1 and reverse shoaled to deep water. Because wave measurements at P_1 were only available during mid-to-high tides, the following analysis only considers runup values measured by the top sensors P_3 and P_4 (Table 3). Corroborating the findings of Stockdon et al. (2006), acceptable but lower correlations were obtained with H_0 measured by the offshore buoy DWR. The highest correlations were obtained with H_0 measured at P_1, suggesting that propagation effects are important. We note that this wave height was derived from pressure measurements in relatively shallow water (0.5–5 m) using linear theory over a flat bottom, which introduces some errors. We further extended this analysis to the choice of the proper period in the parameterization, by comparing η_2 with the five wave periods T_p, $T_{m0,1}$, $T_{m0,2}$, $T_{m0,-1}$, and $T_{m0,-2}$ at DWR, P_0, and P_1 (Table 3). Despite the fact that wave height and period cannot be considered as independent variables, interesting observations can, however, be performed. First of all, we obtained the lowest score with the peak period, regardless the location (not shown here). Therefore, a mean wave period should be preferred over the noisy peak period for runup parameterization, as suggested by several recent studies (Poate et al., 2016; Van der Meer et al., 2016). In general, very similar regressions are obtained with the different mean wave periods, which all show better correlations than T_p. A closer look in Table 3 indicates that, at P_1, better scores are clearly obtained using $T_{m0,-2}$ rather than $T_{m0,2}$ even if both methods show similar performance at DWR. This is likely the result of the spectral transformation during the wave propagation in the nearshore zone, mainly due to nonlinear energy transfers, which reduces the weight of the high-frequency part of the spectrum at the bottom of the cliff (see Figure 7). More generally, these results raise the need to investigate in details the role of the spectral shape and its transformation over intermediate depths in runup parameterization. These changes in the wave spectra are believed to impact the wave runup, and taking them into account through the choice of the mean wave period can improve the skills of empirical runup parameterizations.

Another parameter that has been shown to control the wave runup is the foreshore slope. Runup measurements over uniform structures in laboratory experiments have clearly demonstrated that the wave runup increases with the slope of the structure (Hunt, 1959). However, in natural environments, this runup dependence on slope is more difficult to put in evidence, for several reasons: first, natural beaches are usually characterized by a nonuniform profile, which requires to define the extent over which the slope is computed; second, the slopes encountered on sandy beaches, the most documented natural environment for wave runup studies, represent only a fraction of the full range of slopes encountered along the coasts (e.g., cliffs or coastal structures); third, the alongshore variability and the presence of intertidal and subtidal bars also influence the wave runup and make it difficult to identify the contribution of each parameter. Nevertheless, several studies confirmed the slope dependence of the runup in natural environments (e.g., Nielsen & Hanslow, 1991; Ruggiero et al., 2004; Stockdon et al., 2006). The data we collected on the steep cliffs of Banneg Island shed some lights on the difficulty to compute the foreshore slopes on rocky and irregular environments and thus to interpret the contribution of these slopes to the wave runup. While the correlations between the runup and $\tan\beta\sqrt{H_0 L_0}$ increased when we computed the slopes with methods M_2 and M_3, they actually decreased with the more sophisticated methods M_4 and M_5 that included both the tide and the wave conditions (see section 3.4). It is therefore difficult to draw a comprehensive conclusion on the runup slope dependence on Banneg's cliffs, although previous studies suggest that it should be significant in intermediate-to-reflective environments (Nielsen & Hanslow, 1991; Stockdon et al., 2006). However, a more careful analysis provides some insights on the impact of the topography on the runup, which may explain the spread between

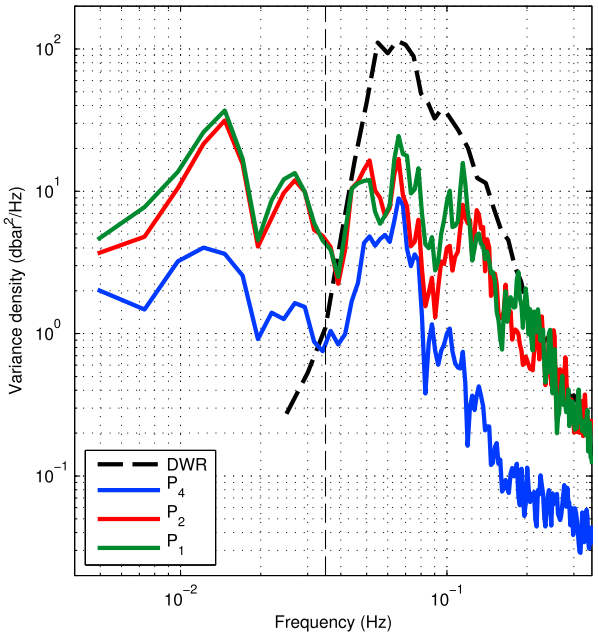

Figure 13. Variance density spectra at P_1, (green line), P_2 (red line), P_4 (blue line), and DWR (black-dashed line) on 5 February 2014, between 8 and 9 A.M. During this event, P_1 was in 0.4-m mean water depth (swash zone), P_2 was in 2.6-m mean water depth, P_4 was in 4.3-m mean water depth, and DWR was in approximately 50-m mean water depth. DWR = Datawell DWR-MkIII.

calculation methods. Note first that the overall cliff profile is concave upward (Figure 2).Therefore, the slope at the breaking will be lower at low tide than at high tide. Based on field measurements and theoretical analysis, Raubenheimer et al. (1996) showed that the ratio of the wave height to the local mean water depth (γ) increased with the beach slope. In our case, the beach curvature should induce a tidal dependence of γ, with lower γ at low tide and higher γ at high tide. Such γ variation is expected to act on the wave energy dissipation (see, e.g., Nielsen, 2009) leading to increased (decreased) dissipation at high (low) tides. The tidal fluctuations of wave dissipation should in turn affect the momentum balance by modifying the gradient of radiation stresses. This will result in a depth dependence of the wave setup, which is the static component of the wave runup. This curvature effect has been described, in an opposite manner, for concave downward site by Becker et al. (2014) and could explain the lower (higher) runup measured at low (high) tide in our case. This effect should be reinforced by the presence of a rocky outcrop at the toe of the cliff, around $X = 55$ m (see Figure 2). This rocky outcrop, as well as the other neighboring terrain features, should certainly act on the wave transformation by increasing dissipation and/or shifting offshore the breaking point. This mechanism is also expected to be depth-dependent, that is, reducing runup for low water level. The overall effect of local bed topography, combining upward concavity and larger-scale reliefs at the toe of the foreshore, can be identified in Figure 11a, for which the slope computed with the baseline method M_1 is identical for all sensors. When comparing measurements performed at each sensor, one notes a general trend of an increase of runup when moving upward. This increase is also clearly visible in the regression functions of η_2 versus $\sqrt{H_0 L_0}$ in Figure 10b. This depth dependence of the runup is compensated by using a sensor-dependent slope calculation, such as observed with the robust regression obtained with M_2 (Figure 11b). However, such an improvement is strongly dependent on the extent of the foreshore considered for the slope calculation: the wider the considered area for slope calculation, the better the regression. Calculations with a large extent will integrate and smooth the effect of curvature, that is, provide similar runup regression for all sensors. This is straightforward for M_2, which uses the largest extent (Figure 12b). For M_3, M_4, and M_5 (Figures 11c–11e), the method dependence to tide and/or wave conditions induces variability in the calculation of tan β due to the displacement along a curved and irregular bed (Figures 12a and 12b). This is particularly true for the lower sensors, for which the slope calculation includes lower parts of the cliff, which involves more pronounced curvature and variability. This clearly results in a worsening of the runup regression. This topography effect is identified in the bimodal behavior observed for M_5, with P_1/P_2 showing much worse regressions than P_3/P_4 (Figure 11e). For M_5, the slope calculation is runup dependent. As the measured runup decreases with increasing water level, the considered segment is also narrower for high water levels. Such smaller extent for slope calculation for P_1/P_2 increases the variability and worsens the regression. All together, these results highlight the role of local topography and slope curvature on the runup dynamics and its depth dependence. Further dedicated high-resolution numerical or laboratory studies are needed to carefully test these observations in controlled conditions.

Of particular interest is the identification of the respective contribution of the wave setup, the incident swash, and the infragravity swash components to the total runup (Guza & Thornton, 1982; Holman & Sallenger, 1985; Stockdon et al., 2006). On Banneg Island, very high infragravity waves, up to 2 m, have been observed (Sheremet et al., 2014). Such infragravity waves are likely to contribute to the occasional flooding of the island and the displacement of cliff-top storm deposits (Autret et al., 2016; Suanez et al., 2009). In order to assess the contribution of these infragravity waves on the wave runup over the cliffs of Banneg Island, we analyzed the pressure signal measured at the bottom of the cliffs (P_1 and P_2) when the sensor at the top of the cliff (P_4) measured some of the highest runup during Petra storm on 5 February 2014. Figure 13 shows the pressure spectra computed from 60-min time series recorded during high tide by the bottom and top sensors. The black line shows the deep-water wave spectra measured at the same time by DWR. Although the spectra at P_1 may be

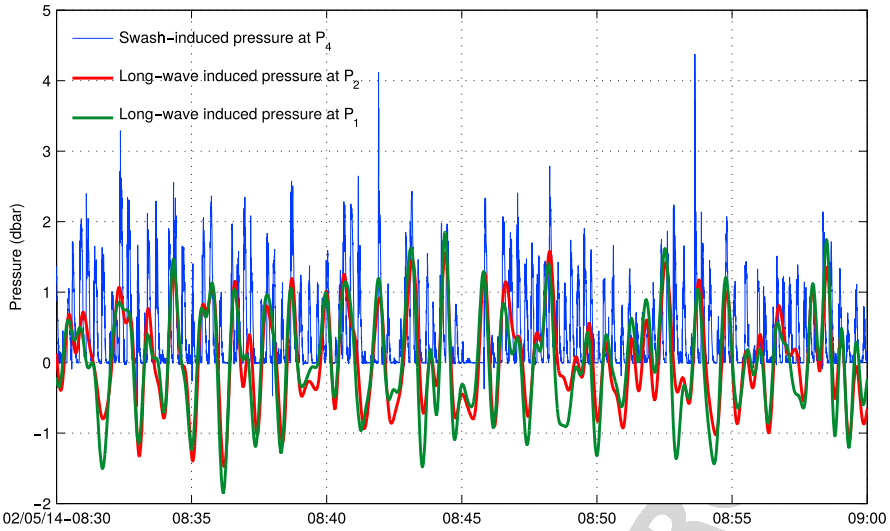

Figure 14. Swash-induced water pressure at P_4 (blue line) and infragravity-wave-induced water pressure at P_1 (green line) and P_2 (red line) on 5 February 2014. The infragravity wave signal was obtained by low-pass (0–0.035 Hz) filtering the pressure signal.

biased because of the truncation of the signal when the sensor is dry, we can clearly see a significant contribution of the energy in the infragravity bands at all three sensors. Looking at the water pressure time series at P_4, superimposed with the infragravity wave signals at P_1 and P_2 (Figure 14), we see that the largest runup events occur quasi-simultaneously with the crest of an infragravity wave at the bottom of the cliff, as if the long waves were acting as carrier waves for the incident short waves. Given the contribution of infragravity waves to the wave runup and the strong alongshore variability in the island morphology, we can assume that the effect of the foreshore slopes on the runup cannot be strictly local, and this, together with topography effects discussed above, contributes to explain the high scatter obtained between η_2 and $\tan\beta\sqrt{H_0L_0}$ when the slope is computed locally as with methods M_4 and M_5.

Stockdon et al. (2006) analyzed wave runup data acquired on sandy beaches and found that the swash was dominated by incident energy for reflective conditions ($\xi_0 > 1.25$). Therefore, they proposed a runup parameterization that does not include the infragravity contribution and linearly depends on $\tan\beta\sqrt{H_0L_0}$ (equation 20 of Stockdon et al., 2006). In this parameterization for reflective conditions, the setup and swash contribute, respectively, to 48% and 52% of the the total runup (values computed from equation 19 in Stockdon et al., 2006). Our experimental setup based on fixed point measurements is not properly designed for such decomposition analysis, for two reasons; first, finer video or lidar-based measurements are required to identify the waterline position, compute the waterline elevation, and decompose the total runup into infragravity and incident components, such as classically done in sandy beaches context; second, the bottom pressure measurements are expected to be significantly affected by nonhydrostatic effects, and conversion into sea surface elevation is likely biased. However, despite these instrument limitations, interesting insight can be gained from the components separation method based on time-series analysis. For this purpose, we identified the first and last 20-min bursts of each immersion cycle, during which the sensor was fully immersed, and we converted the pressure signal into water surface elevation based on the linear theory. The resulting elevation time series were thus measured when the sensor was near the lower limit of the swash zone and were assumed to be a reasonable approximation of the swash elevation. Then, we computed the setup $\overline{\eta}$ as the difference between the 20-min mean elevation and the SWL measured at SBE. We also computed the significant swash height in the incident (S_{inc}) and infragravity (S_{IG}) bands using equation (3) and a separation frequency at 0.035 Hz between the infragravity and the incident bands. The results are depicted in Figure 15, with the setup, the incident swash, the infragravity swash, and the total runup estimated at sensor P_3 against the parameter $\sqrt{H_0L_0}$. First, we note that the total runup (η_2) and the three runup components ($\overline{\eta}$, S_{inc}, and S_{IG}) are well correlated with $\sqrt{H_0L_0}$ indicating a linear relationship between these parameters. Following Stockdon et al. (2006) and writing each runup component as a linear function of $\sqrt{H_0L_0}$, we propose the following

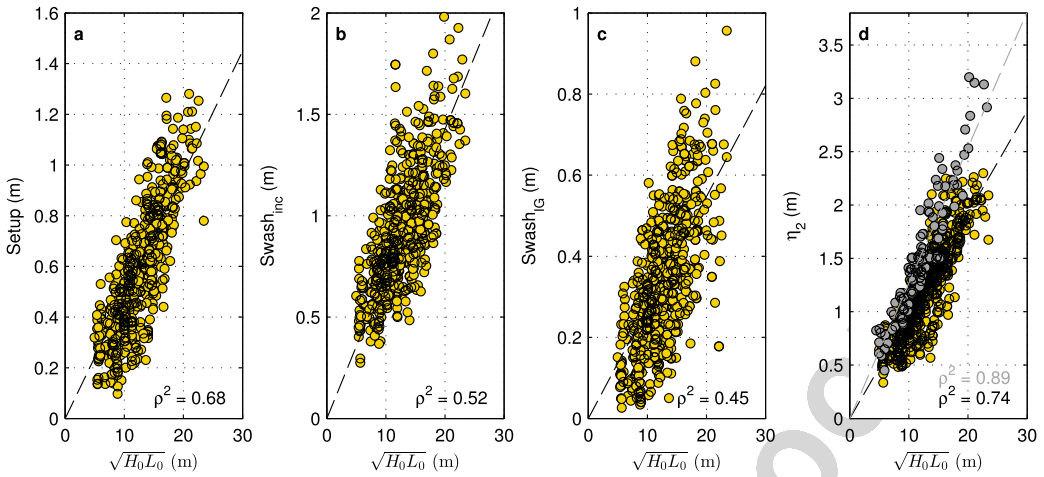

Figure 15. Scatter diagrams of the normalized setup (a), incident swash (b), infragravity swash (c), and $\eta 2$ (d) versus ξ_0, with the foreshore slope computed either with method 2, at P_3.

relationship for η_2,

$$\eta_2 = 1.1\left(\overline{\eta} + \frac{\sqrt{S_{inc}^2 + S_{IG}^2}}{2}\right) = 1.1K_1\sqrt{H_0L_0} + 0.55\sqrt{K_2^2 + K_3^2}\sqrt{H_0L_0} = K\sqrt{H_0L_0}. \quad (7)$$

where K_1 (0.048), K_2 (0.071), K_3 (0.027), and K (0.096) are the slopes of the linear regressions with a null intercept for $\overline{\eta}$, S_{inc}, S_{IG} and η_2, respectively. The fact that $1.1K_1 + 0.55\sqrt{K_2^2 + K_3^2}$ (0.095) is very close to K (0.096) supports the decomposition of the total runup given in equation (7). With this parameterization, we see that the setup and the swash contribute to 56% and 44% of the total runup η_2, while Stockdon et al. (2006) obtained 48% and 52%, respectively. Therefore, our wave runup observations tend to show that the contribution of the wave setup could be underestimated by the formula proposed by these authors, when applied to steep rocky cliff environments. In addition, the swash component is clearly dominated by the incident band, as expected in our steep slope context. However, these results need to be considered cautiously, given the strong assumptions mentioned above. A comparison between the total η_2 calculated with the threshold method defined in section 3.3 (gray circles) and with the time-series approach used herein (yellow circles) is shown in Figure 15d. The significant difference in the regression slopes (the slope obtained with the threshold approach is 32% larger than one obtained with the time-series approach) shows the fragility of the time-series approach in our context and highlights the robustness of our initial strategy, which provides much better regression. Therefore, future work on steep rock cliffs based on lidar or video measurements will be necessary to determine with more confidence the relative contribution of setup and swash on total runup in such environments.

Finally, the overall good fit between η_2 and $\tan\beta\sqrt{H_0L_0}$, obtained with all methods except M_5 (see Figure 11 and discussion here above), revealed a linear relationship between these parameters. Yet a direct comparison with the more commonly used equations for R_2 predictions, such as the ones of Holman and Sallenger (1985) or Stockdon et al. (2006), was not applicable to our data set because of the difference between η_2, the 2% exceedance level of shoreline elevation, and R_2, the 2% exceedance level of runup maxima. Holland and Holman (1993) found that the distribution of swash maxima could be approximated with a Rayleigh distribution (Cartwright & Longuet-Higgins, 1956), derived for sea waves treated as a linear superposition of random Gaussian waves with a narrow spectrum. However, they observed systematic non-Gaussian deviations in the statistics describing the upper tail of the distributions. Further investigations are thus required to better understand the statistical distribution of swash maxima and to define a relation between η_2 and R_2. Holman (1986) analyzed video-based runup measurements on a mild-sloping beach with foreshore slopes comprised between 0.07 and 0.2. During his experiment, the incident wave height varied from 0.4 to 4.0 m, the peak period varied from 6 to 16 s, and the resulting Iribarren number varied from 0.5 to 4.0. The conditions that we numerically reproduced on Banneg Island (at P_0) covered a slightly wider range with incident wave heights

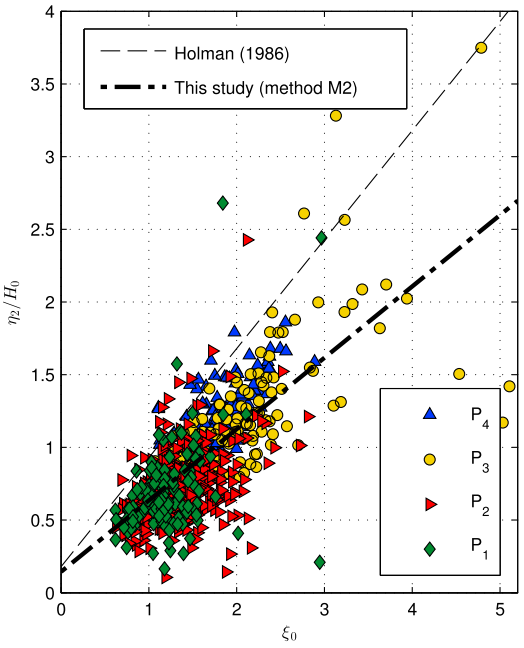

Figure 16. Scatter diagrams of η_2/H_0 versus ξ_0 with the foreshore slope computed with M_2.

comprised between 0.2 and 5.3 m, peak periods comprised between 5 and 20 s, and Iribarren number comprised between 0.2 and 5.0. Holman (1986) computed the relationships between the surf-similarity parameter ξ_0 and several statistical parameters for extreme wave runup, including η_2. He obtained the following linear relation for the nondimensional η_2

$$\frac{\eta_2}{H_0} = 0.75\xi_0 + 0.18, \tag{8}$$

and related the positive intercept 0.18 to the wave setup. With our data, the regression slopes (0.14, 0.49, 0.19, 0.07, and 0.14, for methods 1 to 5, respectively) were systematically lower than the one obtained by (Holman, 1986; 0.75), and the intercepts were comprised between 0.14 and 0.75. Figure 16 shows η_2/H_0 against ξ_0 computed with method M_2, for which the best fit was obtained. Obviously, there is a strong impact on the results of the selected method to compute the foreshore slopes, making the interpretation of the regression analysis difficult (see Figure 11). The difference between well-documented sandy beaches and the steep rocky cliffs investigated herein should result from the combination of a range of processes, which are difficult to discriminate with the present setup and will require further dedicated field studies. Following the recent work of Poate et al. (2016), the stronger steepness should lead to increased values of runup. The opposite is observed here, which highlights the role played by the complex terrain features on the overall wave transformation. Following the general understanding of turbulent boundary layers in open channel flows (Rosman & Hench, 2011; Tachie et al., 2000) or recent works on wave dynamics over coral reefs (Monismith et al., 2015; Pomeroy et al., 2012; Van Dongeren et al., 2013), the bottom roughness is expected to enhance energy dissipation, and this effect increases with the height of roughness elements relative to the local water depth. Furthermore, when the physical roughness height increases to more than few percents of the water depth, the concept of bottom roughness itself becomes irrelevant, and the flow and wave dynamics must be discussed in the framework of porous media (Arnaud et al., 2017; Monismith, 2014). The quantitative comparison between runup over coral reefs and rocky cliff is not directly relevant, as shorelines in coral reef systems are separated from the steep forereef by a reef flat and/or lagoon. However, interesting insight can be gained from the existing information on wave dynamics above the outer part of the coral reef, from the forereef to the reef crest, where most of the wave transformation occurs in quite comparable conditions to our system both in terms of slope or roughness. At the reef scale, classical linear wave theory appears to provide the good description of wave transformation (Monismith et al., 2013). Finer laboratory studies on wave setup over rough fringing reefs reveal the presence of two competing effects acting on the momentum balance (Buckley et al., 2016). On one hand, the frictional dissipation due to increased bottom roughness offshore of the breaking point tends to reduce the wave heights prior to wave breaking and consequently reduce the wave setup compared to the smooth case. On the other hand, the offshore-directed shear stress due to wave-current interaction acts to increase the wave setup. Both processes are nearly in balance in the laboratory experiments of Buckley et al. (2016) . Such processes acting on the shoaling and surf zone dynamics are certainly important in our field case and may contribute to explain part of the observed runup reduction in comparison to the smooth and mild slope beach case of Holman (1986). The quantification of their relative contribution will require further dedicated studies. Further onshore, the presence of macroroughness drastically affects the breaking waves and swash tongues through impacts, rebounds, and splash-ups inducing a violently aerated and turbulent flow structure. In addition, infiltration processes could affect the runup dynamics by inducing a net volume loss. So far, the precise understanding of the involved processes is still out of reach for experimental field research works, and most of the knowledge is gained from high-resolution numerical modeling (Losada et al., 2008; Sambe et al., 2011; Torres-Freyermuth et al., 2013). In a more applied perspective, Van der Meer et al. (2016) discuss the runup attenuation over rock armor rubble-mound breakwaters, probably the documented environment that most resembles Banneg's rocky cliffs. Based on the laboratory experiments of Van der Meer and Stam (1992), they mention attenuation factors comprised between 0.38 and 0.6, depending on the number of rock layers, the type of rocks, and the permeability of the structure. If we compare the

regression slopes of the linear relationship, we derived for Banneg's cliff with the one obtained by Holman (1986); on sandy beach, we obtain attenuation factor of similar order of magnitude, comprised between 0.09 and 0.65 depending on the method used to compute the cliff slope. These considerations raise the need to further investigate wave physics on steep and rough environments, which includes rocky cliffs and coral reefs, in order to better discriminate the involved processes related to wave transformation and swash propagation and improve the accuracy of extreme runup predictions for such environments.

6. Conclusion

For the first time, observations of wave runup over natural rocky cliffs are presented. Measurements from pressure sensors deployed in the intertidal zone of Banneg Island were processed to derive the 2% exceedance level of water elevation η_2 at discrete time and specific locations. Runup estimates were obtained for a wide range of wave conditions and tidal phases. They showed a strong correlation with the parameter $\sqrt{H_0 L_0}$ ($\rho^2 = 0.72$), particularly when H_0 was taken in the nearshore and reverse-shoaled to an equivalent deep-water value. L_0 was computed from the wave period based on the linear theory. The best correlations between η_2 and $\sqrt{H_0 L_0}$ were obtained when we computed L_0 from the integrated period $T_{m0,-2}$, which is less noisy than the usual peak period T_p and reduces the weight of the high-frequency part of the wave energy spectrum. Given the macrotidal regime of the study area and the irregular profile of the instrumented cliff, the foreshore slope significantly varied ($0.1 < \tan\beta < 0.4$) between runup measurements. In order to assess its impact on the wave runup, several methods for slope computation were adapted from existing techniques developed for natural sandy and gravel environments. Although improved correlations between η_2 and $\tan\beta\sqrt{H_0 L_0}$ were obtained when the slope was computed over a fixed segment that only depended on the runup height, we obtained weaker correlations with methods that take into account the tidal phase and the wave conditions. The lower accuracy of the runup regressions based on wave-dependent slope calculations as well as the runup depth dependence are mostly attributed to the effect of local bed topography. The concave upward curvature of the foreshore combined with the presence of large terrain relief at the base of the cliff induces a runup increase for high water level and, on a methodological point of view, highlights the need to integrate the whole foreshore in the slope calculation rather than to use wave-dependent slope calculations. The assumption that infragravity waves significantly contribute to the most extreme wave runup, as supported by Sheremet et al. (2014), was verified here based on data recorded during a major storm event. The large scale and alongshore variability of infragravity waves may explain the absence of runup dependence on local foreshore slopes. Despite the fragility of such single-point analysis in our context, additional time-series analysis reveals the dominant contribution of wave setup and incident swash to the total runup. Finally, regression analysis of the nondimensional runup against the surf-similarity parameter showed a significant attenuation of the wave runup on the rocky cliffs of Banneg Island in comparison to sandy beach profiles (Holman, 1986). This result is in-line with laboratory and numerical studies of wave runup over rock armor breakwaters. Further work will be needed in order to determine the combined contributions of enhanced drag forces by bottom roughness and water infiltration on the dynamics of wave runup over fractured rocky media.

Acknowledgments
We warmly thank the Réserve naturelle d'Iroise and its rangers H. Maheo and D. Bourles for allowing us to perform the measurements and helping in many ways to access the site. Many thanks also go to the technical group at the French Navy Hydrographic and Oceanographic Institute (SHOM) who deployed and recovered the instruments. This work is part of the research program PROTEVS (research contract 12CR6) funded by DGA and conducted by SHOM. This research is also supported by the "Laboratoire d'Excellence" LabexMER (ANR-10-LABX-19) and cofunded by the French government under the program "Investissements d'Avenir," and the region of Brittany. The Litto3D coastal elevation model used for this study is coproduced by IGN and SHOM from lidar and MBES surveys and is available on http://diffusion.shom.fr/pro/risques/altimetrie-littorale/litto3dr-finistere-2014.html. The wave parameters at *Les Pierres Noires* buoy were extracted from the French wave measurement network CANDHIS website (http://candhis.cetmef.developpement-durable.gouv.fr/). The long-term wave model results were extracted from the HOMERE hindcast database available at https://forms.ifremer.fr/lops-oc/marc-homere/. The raw OSSI and DWR data collected during the PROTEVS field campaigns are available on ftp://shom2jgr:ShohT7ya@ftp.shom.fr. In addition, all the processed data used for the analysis and the generation of the figures are provided as supporting information (Dodet et al., 2018).

References

Ardhuin, F., Rawat, A., & Aucan, J. (2014). A numerical model for free infragravity waves: Definition and validation at regional and global scales. *Ocean Modelling*, *77*, 20–32. https://doi.org/10.1016/j.ocemod.2014.02.006

Ardhuin, F., Rogers, E., Babanin, A. V., Filipot, J.-F., Magne, R., Roland, A., et al. (2010). Semiempirical dissipation source functions for ocean waves. Part I: Definition, calibration, and validation. *Journal of Physical Oceanography*, *40*(9), 1917–1941. https://doi.org/10.1175/2010JPO4324.1

Ardhuin, F., Roland, A., Dumas, F., Bennis, A.-C., Sentchev, A., Forget, P., et al. (2012). Numerical wave modeling in conditions with strong currents: Dissipation, refraction, and relative wind. *Journal of Physical Oceanography*, *42*(12), 2101–2120. https://doi.org/10.1175/JPO-D-11-0220.1

Arnaud, G., Rey, V., Touboul, J., Sous, D., Molin, B., & Gouaud, F. (2017). Wave propagation through dense vertical cylinder arrays: Interference process and specific surface effects on damping. *Applied Ocean Research*, *65*, 229–237. https://doi.org/10.1016/j.apor.2017.04.011

Atkinson, A. L., Power, H. E., Moura, T., Hammond, T., Callaghan, D. P., & Baldock, T. E. (2017). Assessment of runup predictions by empirical models on non-truncated beaches on the south-east Australian coast. *Coastal Engineering*, *119*, 15–31. https://doi.org/10.1016/j.coastaleng.2016.10.001

Autret, R., Dodet, G., Fichaut, B., Suanez, S., David, L., Leckler, F., et al. (2016). A comprehensive hydro-geomorphic study of cliff-top storm deposits on Banneg Island during winter 2013–2014. *Marine Geology*, *382*, 37–55. https://doi.org/10.1016/j.margeo.2016.09.014

Battjes, J., & Janssen, J. (1978). Energy loss and set-up due to breaking of random waves, *Proceedings of the 16th International Conference on Coastal Engineering*. New-York: ASCE, pp. 569–587.

Battjes, J. A. (1974). Surf similarity, *Proceedings of the 14th International Conference on Coastal Engineering*: ASCE, pp. 466–480.

Becker, J. M., Merrifield, M. A., & Ford, M. (2014). Water level effects on breaking wave setup for Pacific Island fringing reefs. *Journal of Geophysical Research: Oceans*, *119*, 914–932. https://doi.org/10.1002/2013JC009373

Blenkinsopp, C. E., Matias, A., Howe, D., Castelle, B., Marieu, V., & Turner, I. L. (2016). Wave runup and overwash on a prototype-scale sand barrier. *Coastal Engineering*, *113*, 88–103. https://doi.org/10.1016/j.coastaleng.2015.08.006

Boudière, E., Maisondieu, C., Ardhuin, F., Accensi, M., Pineau-Guillou, L., & Lepesqueur J. (2013). A suitable metocean hindcast database for the design of marine energy converters. *International Journal of Marine Energy*, *3-4*, e40–e52. https://doi.org/10.1016/j.ijome.2013.11.010

Buckley, M. L., Lowe, R. J., Hansen, J. E., & Van Dongeren, A. R. (2016). Wave setup over a fringing reef with large bottom roughness. *Journal of Physical Oceanography*, *46*(8), 2317–2333. https://doi.org/10.1175/JPO-D-15-0148.1

Cartwright, D. E., & Longuet-Higgins, M. S. (1956). The statistical distribution of the maxima of a random function. *Proceedings of the Royal Society of London. Series A, Mathematical and Physical Sciences*, *237*(1209), 212–232.

Dodet, G., Leckler, F., Sous, D., Ardhuin, F., Filipot, J.-F., & Suanez, S. (2018). Supporting information for "Wave runup over steep rocky cliffs." *Journal of Geophysical Research: Oceans*, 1–3.

Eldeberky, Y., Technische Hogeschool Delft, & Afdeling der Civiele Techniek (1996). *Nonlinear transformation of wave spectra in the nearshore zone*. Delft, Netherlands: Faculty of Civil Engineering, Delft University of Technology.

Fichaut, B., & Hallégouët, B. (1989). Banneg, une île dans la tempête. *Penn ar Bed*, *135*, 36–43.

Fichaut, B., & Suanez, S. (2011). Quarrying, transport and deposition of cliff-top storm deposits during extreme events: Banneg Island, Brittany. *Marine Geology*, *283*(1-4), 36–55. https://doi.org/10.1016/j.margeo.2010.11.003

Guza, R. T., & Thornton, E. B. (1982). Swash oscillations on a natural beach. *Journal of Geophysical Research*, *87*(C1), 483–491. https://doi.org/10.1029/JC087iC01p00483

Hasselmann, S., & Hasselmann, K. (1985). Computations and parameterizations of the nonlinear energy transfer in a gravity-wave spectrum. Part I: A new method for efficient computations of the exact nonlinear transfer integral. *Journal of Physical Oceanography*, *15*(11), 1369–1377. https://doi.org/10.1175/1520-0485(1985)015<1369:CAPOTN>2.0.CO;2

Hesser, T., Smith, J. M., Bryant, M. A., & Roland, A. (2018). Nearshore validation of unstructured WAVEWATCH III, *Ocean Sciences Meeting*: AGU.

Holland, K. T., & Holman, R. A. (1993). The statistical distribution of swash maxima on natural beaches. *Journal of Geophysical Research*, *98*(C6), 10271–10278. https://doi.org/10.1029/93JC00035

Holland, K. T., Raubenheimer, B., Guza, R. T., & Holman, R. A. (1995). Runup kinematics on a natural beach. *Journal of Geophysical Research*, *100*(C3), 4985–4993. https://doi.org/10.1029/94JC02664

Holman, R. A. (1986). Extreme value statistics for wave run-up on a natural beach. *Coastal Engineering*, *9*(6), 527–544. https://doi.org/10.1016/0378-3839(86)90002-5

Holman, R. A., & Guza, R. T. (1984). Measuring run-up on a natural beach. *Coastal Engineering*, *8*(2), 129–140. https://doi.org/10.1016/0378-3839(84)90008-5

Holman, R. A., & Sallenger, A. H. (1985). Setup and swash on a natural beach. *Journal of Geophysical Research*, *90*(C1), 945–953. https://doi.org/10.1029/JC090iC01p00945

Hunt, I. (1959). Design of seawalls and breakwaters. *Journal of the Waterways and Harbors Division*, *85*(3), 123–152.

Huntley, D. A., Guza, R. T., & Bowen, A. J. (1977). A universal form for shoreline run-up spectra? *Journal of Geophysical Research*, *82*(18), 2577–2581. https://doi.org/10.1029/JC082i018p02577

Lazure, P., & Dumas, F. (2008). An external–internal mode coupling for a 3D hydrodynamical model for applications at regional scale (MARS). *Advances in Water Resources*, *31*(2), 233–250. https://doi.org/10.1016/j.advwatres.2007.06.010

Leckler, F., Roland, A., Dutour-Sikiric, M., Ardhuin, F., Michaud, H., Huchet, J.-F. Filipot, & Dodet, G. (2016). Multi-scale resolution modeling in WAVEWATCH III with triangle-based meshes: Explicit and implicit schemes in versions 4.18 & 5.xx with application to the Iroise sea, *WISE Meeting*. Italy: Venice.

Losada, I. J., Lara, J. L., Guanche, R., & Gonzalez-Ondina, J. M. (2008). Numerical analysis of wave overtopping of rubble mound breakwaters. *Coastal Engineering*, *55*(1), 47–62. https://doi.org/10.1016/j.coastaleng.2007.06.003

Louvart, L., & Grateau, C. (2005). The Litto3D project. *Europe Oceans 2005*, *2*, 1244–1251. https://doi.org/10.1109/OCEANSE.2005.1513237

Masselink, G., Castelle, B., Scott, T., Dodet, G., Suanez, S., Jackson, D., & Floc'h, F. (2016). Extreme wave activity during 2013/2014 winter and morphological impacts along the Atlantic coast of Europe. *Geophysical Research Letters*, *43*, 2135–2143. https://doi.org/10.1002/2015GL067492

Monismith, S. G. (2014). Flow through a rough, shallow reef. *Coral Reefs*, *33*(1), 99–104. https://doi.org/10.1007/s00338-013-1107-0

Monismith, S. G., Herdman, L. M. M., Ahmerkamp, S., & Hench, J. L. (2013). Wave transformation and wave-driven flow across a steep coral reef. *Journal of Physical Oceanography*, *43*(7), 1356–1379. https://doi.org/10.1175/JPO-D-12-0164.1

Monismith, S. G., Rogers, J. S., Koweek, D., & Dunbar, R. B. (2015). Frictional wave dissipation on a remarkably rough reef. *Geophysical Research Letters*, *42*, 4063–4071. https://doi.org/10.1002/2015GL063804

Nielsen, P. (2009). Coastal and estuarine processes. *Advanced Series on Ocean Engineering (World Scientific)*, *29*(4).

Nielsen, P., & Hanslow, D. J. (1991). Wave runup distributions on natural beaches. *Journal of Coastal Research*, *7*(4), 1139–1152.

Pineau-Guillou, L., Dumas, F., Theetten, S., Ardhuin, F., Le Roux, J.-F., et al. (2014). PREVIMER: Improvement of surge, sea level and currents modelling. *Mercator Ocean — Quarterly Newsletter*, *49*, 29–38.

Poate, T. G., McCall, R. T., & Masselink, G. (2016). A new parameterisation for runup on gravel beaches. *Coastal Engineering*, *117*, 176–190. https://doi.org/10.1016/j.coastaleng.2016.08.003

Pomeroy, A., Lowe, R., Symonds, G., Van Dongeren, A., & Moore, C. (2012). The dynamics of infragravity wave transformation over a fringing reef. *Journal of Geophysical Research*, *117*(C11), C11022. https://doi.org/10.1029/2012JC008310

Raubenheimer, B., & Guza, R. T. (1996). Observations and predictions of run-up. *Journal of Geophysical Research*, *101*(C11), 25575–25587. https://doi.org/10.1029/96JC02432

Raubenheimer, B., Guza, R. T., & Elgar, S. (1996). Wave transformation across the inner surf zone. *Journal of Geophysical Research*, *101*(C11), 25589–25597. https://doi.org/10.1029/96JC02433

Roland, A. (2009). Spectral wave modelling on unstructured meshes (Ph.D. thesis).

Roland, A., & Ardhuin, F. (2014). On the developments of spectral wave models: Numerics and parameterizations for the coastal ocean. *Ocean Dynamics*, *64*(6), 833–846. https://doi.org/10.1007/s10236-014-0711-z

Rosman, J. H., & Hench, J. L. (2011). A framework for understanding drag parameterizations for coral reefs. *Journal of Geophysical Research*, *116*(C8), C08025. https://doi.org/10.1029/2010JC006892

Ruessink, B. G., Kleinhans, M. G., & van den Beukel, P. G. L. (1998). Observations of swash under highly dissipative conditions. *Journal of Geophysical Research*, *103*(C2), 3111–3118. https://doi.org/10.1029/97JC02791

Ruggiero, P., Holman, R., & Beach, R. (2004). Wave run-up on a high-energy dissipative beach. *Journal of Geophysical Research*, *109*. https://doi.org/10.1029/2003JC002160

SHOM (2014). *Réfénces Altimétriques Maritimes. Côtes du zéro hydrographique et niveaux caractéristiques de la marée*. Brest: Service hydrographique et océanographique de la Marine.

Sambe, A. N., Sous, D., Golay, F., Fraunié, P., & Marcer, R. (2011). Numerical wave breaking with macro-roughness. *European Journal of Mechanics — B/Fluids*, *30*(6), 577–588. https://doi.org/10.1016/j.euromechflu.2011.03.002

Senechal, N., Coco, G., Bryan, K. R., & Holman, R. A. (2011). Wave runup during extreme storm conditions. *Journal of Geophysical Research: Oceans*, *116*(C7), C07032. https://doi.org/10.1029/2010JC006819

Sheremet, A., Staples, T., Ardhuin, F., Suanez, S., & Fichaut, B. (2014). Observations of large infragravity wave runup at Banneg Island, France. *Geophysical Research Letters*, *41*, 976–982. https://doi.org/10.1002/2013GL058880

Smith, J. M., Hesser, T., Bryant, M. A., Roland, A., & Dutour-Sikiric, M. (2017). Evaluation of unstructured WAVEWATCH III for nearshore application, 1st workshop on waves, storm surges and coastal hazards, Liverpool.

Stockdon, H. F., Holman, R. A., Howd, P. A., & Sallenger Jr, A. H. (2006). Empirical parameterization of setup, swash, and runup. *Coastal Engineering*, *53*(7), 573–588. https://doi.org/10.1016/j.coastaleng.2005.12.005

Suanez, S., Cancouët, R., Floc'h, F., Blaise, E., Ardhuin, F., Filipot, J.-F., et al. (2015). Observations and predictions of wave runup, extreme water levels, and medium-term dune erosion during storm conditions. *Journal of Marine Science and Engineering*, *3*(3), 674–698. https://doi.org/10.3390/jmse3030674

Suanez, S., Fichaut, B., & Magne, R. (2009). Cliff-top storm deposits on Banneg Island, Brittany, France: Effects of giant waves in the eastern atlantic ocean. *Sedimentary Geology*, *220*(1-2), 12–28. https://doi.org/10.1016/j.sedgeo.2009.06.004

Tachie, M. F., Bergstrom, D. J., & Balachandar, R. (2000). Rough wall turbulent boundary layers in shallow open channel flow. *Journal of Fluids Engineering*, *122*(3), 533–541. https://doi.org/10.1115/1.1287267

Tolman, H. L. (2014). User manual and system documentation of WAVEWATCH III version 4.18. *NOAA/NWS/NCEP/MMAB Technical Note*, *316*(276), 194.

Torres-Freyermuth, A., Puleo, J. A., & Pokrajac, D. (2013). Modeling swash-zone hydrodynamics and shear stresses on planar slopes using Reynolds-averaged Navier-Stokes equations. *Journal of Geophysical Research: Oceans*, *118*, 1019–1033. https://doi.org/10.1002/jgrc.20074

Van Dongeren, A., Lowe, R., Pomeroy, A., Trang, D. M., Roelvink, D., Symonds, G., & Ranasinghe, R. (2013). Numerical modeling of low-frequency wave dynamics over a fringing coral reef. *Coastal Engineering*, *73*, 178–190. https://doi.org/10.1016/j.coastaleng.2012.11.004

Van der Meer, J. W., Allsop, N., Bruce, T., De Rouck, J., Kortenhaus, A., Pullen, T., et al. (2016). EurOtop, 2016. Manual on wave overtopping of sea defences and related structures. An overtopping manual largely based on European research, but for worldwide application (*Tech. rep.*): European Overtopping Manual.

Van der Meer, J. W., & Stam, C.-J. M. (1992). Wave runup on smooth and rock slopes of coastal structures. *Journal of Waterway, Port, Coastal, and Ocean Engineering*, *118*(5), 534–50. https://doi.org/10.1061/(ASCE)0733-950X(1992)118:5(534)

Vousdoukas, M. I., Wziatek, D., & Almeida, L. P. (2012). Coastal vulnerability assessment based on video wave run-up observations at a mesotidal, steep-sloped beach. *Ocean Dynamics*, *62*(1), 123–137. https://doi.org/10.1007/s10236-011-0480-x

Young, I. R., Verhagen, L. A., & Banner, M. L. (1995). A note on the bimodal directional spreading of fetch-limited wind waves. *Journal of Geophysical Research*, *100*(C1), 773–778. https://doi.org/10.1029/94JC02218